

Direct visualization of an elusive molecular reaction: Time-resolved H₂ roaming in acetonitrile

Debadarshini Mishra*^{†,1} Aaron C. LaForge*^{†,1} Lauren M. Gorman,¹
Sergio Díaz-Tendero,^{2,3,4} Fernando Martín,^{2,3,5} and Nora Berrah¹

¹*Department of Physics, University of Connecticut, Storrs, Connecticut, 06269, USA**

²*Departamento de Química, Módulo 13, Universidad Autónoma de Madrid, 28049 Madrid, Spain, EU*

³*Condensed Matter Physics Center (IFIMAC), Universidad Autónoma de Madrid, 28049 Madrid, Spain, EU*

⁴*Institute for Advanced Research in Chemical Sciences (IAdChem),
Universidad Autónoma de Madrid, 28049 Madrid, Spain*

⁵*Instituto Madrileño de Estudios Avanzados en Nanociencia (IMDEA-Nano),
Campus de Cantoblanco, 28049 Madrid, Spain, EU*

(Dated: July 4, 2023)

We introduce a novel approach to imaging the complex phenomenon of roaming, an unconventional mechanism that contributes to molecular dissociation. During roaming, fragments remain weakly-bound to each other due to long-range electrostatic interactions. This extended period of interaction time allows for the formation of new molecular compounds. However, the neutral character of the roaming fragment and its indeterminate trajectory have made it difficult to experimentally identify and systematically study. To address this challenge, we utilize intense, femtosecond IR radiation in combination with coincident Coulomb explosion imaging to directly reconstruct the momentum vector of the neutral roaming H₂ from ionized acetonitrile, CH₃CN. This technique not only provides a kinematically complete picture of the underlying molecular dynamics that contribute to H₃⁺ formation, but more significantly, yields an unambiguous experimental signature of roaming. We corroborate this with the aid of quantum chemistry calculations, which allow us to fully determine how this unique dissociative process occurs. Our method enables a direct visualization of roaming reactions, making the investigation of this complex process more feasible.

INTRODUCTION

Understanding the multitude of complex molecular processes proceeding through photoexcitation is of fundamental importance to a wide variety of biological and chemical systems. Dissociation, one of the more common photochemical processes, typically proceeds by the fragmenting molecule moving along the path of minimum energy. However, there exists a more indirect pathway, known as roaming, where the neutral fragment explores the relatively flat regions of the potential energy surface far from the minimum energy path due to long-range, weakly-bound interactions. As the name suggests, the indirect nature of dissociation through roaming makes this channel more complex than the more typical fragmentation channels. That said, roaming has been a subject of great interest in recent years [1–3]. From its initial indirect observation in formaldehyde [4], roaming has been proposed to occur in several small molecules such as acetaldehyde [5, 6], acetone [7], nitrate [8], methyl formate [9, 10], and propane [11]. Recently, roaming of H₂ in monohydric alcohols, initiated by intense femtosecond laser pulses, was shown to lead to H₃⁺ formation [12–14]. In general, photoexcitation of organic molecules, using

high-powered, ultrafast lasers, has proven to be an efficient means to produce H₃⁺ [15–21]. Additionally, H₃⁺, an abundant cation in interstellar media [22, 23], is of great interest due to its importance in gas-phase chemistry where it plays a critical role in the production of more complex molecules [24].

Although roaming has been proposed to occur in a multitude of small molecules, a direct visualization of roaming has remained elusive from experimental observations due to its complex nature. The central problem is the random nature of the roaming process itself, where the relative position of the roaming particle with respect to the rest of the system is not deterministic. For instance, pioneering experimental studies [12–14] inferred the role of roaming neutral H₂ in the H₃⁺ formation process by relying heavily on simulations. These studies could not fully exploit the potential of coincident momentum imaging, which is crucial in distinguishing a true experimental signature for roaming from other fragmentation processes. More recently, Endo *et al.* [25] demonstrated time-resolved signature of roaming in formaldehyde by investigating a three-ion coincidence channel using Coulomb explosion imaging (CEI). However, this channel carries imprints of various reactions that are triggered via UV excitation of formaldehyde, including molecular and radical dissociation, as well as roaming. As a result, it was necessary to incorporate high-level simulations to identify the signature of roam-

[†] To whom correspondence should be addressed. Email: debadarshini.mishra@uconn.edu or aaron.laforge@uconn.edu

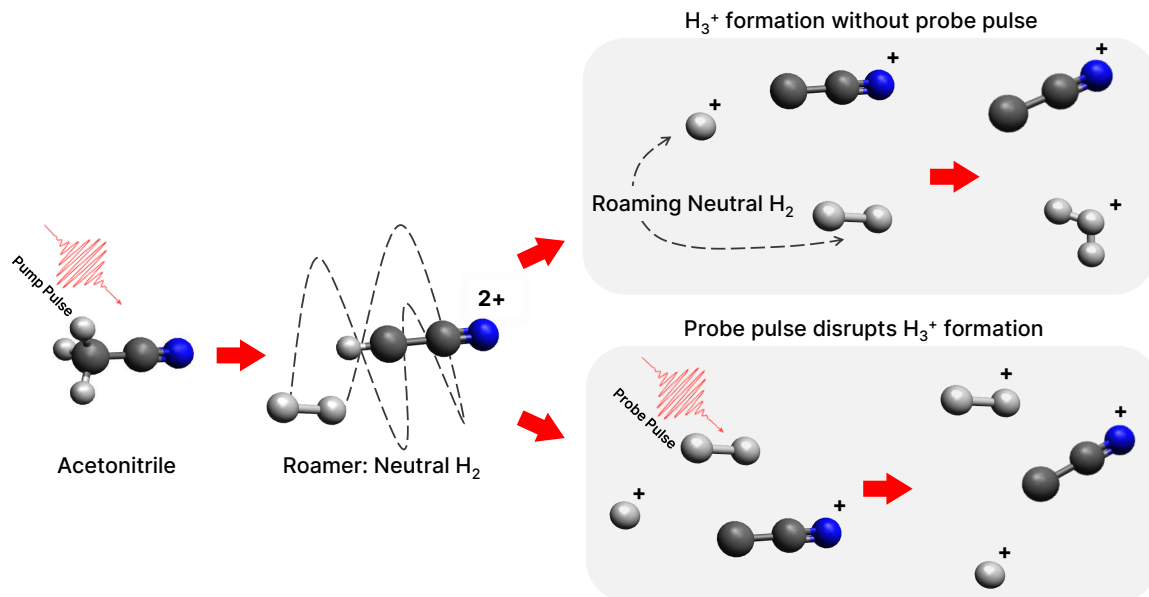


Figure 1. Schematic of H_2 roaming and H_3^+ formation in CH_3CN . The pump pulse creates $[\text{CH}_3\text{CN}]^{2+}$ by multiphoton absorption followed by neutral fragmentation of H_2 . Some H_2 remains weakly-bound to the dication in a roaming state. Afterward, an H^+ is abstracted from the dication forming H_3^+ . If the time-delayed probe pulse arrives before abstraction, the process prevents H_3^+ formation.

ing from the experimental results.

In this paper, we conduct a systematic, time-resolved investigation of the formation of H_3^+ in acetonitrile, CH_3CN , by directly tracking the dynamics of the roaming neutral H_2 , which is ‘invisible’ to charged-particle detection schemes. We make use of coincident momentum imaging in combination with femtosecond IR-IR pump-probe spectroscopy. This allows us to access the full, time-resolved 3D momentum information of each detected fragment, while also enabling us to reconstruct the momentum vector of the undetected neutral or ‘invisible’ fragment in the reaction, by virtue of momentum conservation. Such kinematically complete information, even for a coincidence channel involving a neutral fragment, is crucial for mapping out a direct signature of roaming reactions, without any interference from other excited state dynamics. Furthermore, the choice of acetonitrile for our current study makes the analysis of H_3^+ formation easier, since it only has three hydrogen atoms that are bonded to the same carbon atom, thereby avoiding complications that may arise with molecules that have more than three hydrogen atoms. A schematic of H_2 roaming and H_3^+ formation in CH_3CN is given in Fig. 1. We produce the parent dicationic state with an intense, femtosecond pump pulse. H_3^+ is formed as a result of a roaming H_2 neutral which remains in the flat part of the potential energy surface before abstracting a hydrogen ion from the parent molecule. The formation of H_3^+ is probed with a time-delayed fs pulse that disrupts the ensuing

dynamics by ionizing the neutral H_2 , thereby preventing the formation of H_3^+ and depleting its yield. A more in-depth discussion of our specific experimental setup is given in the Methods section. The momenta of the resulting ionic fragments from the laser-molecule interaction are measured in coincidence using the COLTRIMS technique [26, 27].

RESULTS AND DISCUSSION

To elucidate the role of H_2 roaming in the formation of H_3^+ in photoionized acetonitrile, we begin by investigating its kinematically complete time-resolved dynamics. Fig. 2 (a) shows the complete KER map of the channel $\text{H}_3^+ + \text{C}_2\text{N}^+$ as a function of pump-probe delay while (b) shows the projection of the KER band between 3 eV and 7 eV. We primarily observe a horizontal band centered around a KER of 5 eV, due to a single pulse exciting the molecule directly into the dicationic state. Typically, these types of KER maps show a dynamic, energy-dependent behavior with respect to pump-probe delay. In that case, the pump pulse excites the system into the ionic state and the time-delayed probe pulse further ionizes the system into a higher charged state, resulting in a mapping of the kinetic energy from Coulomb repulsion as a function of time. In contrast, here we only observe a very weak energy-dependent behavior in the KER map, since the formation of H_3^+ is induced directly through

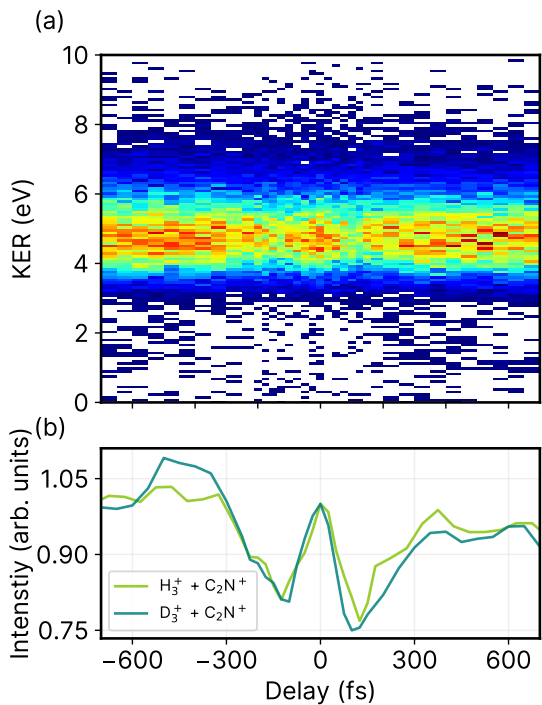


Figure 2. (a) Time-dependent kinetic energy release of $\text{H}_3^+ + \text{C}_2\text{N}^+$. (b) Projection of KER signal for $\text{H}_3^+ + \text{C}_2\text{N}^+$ (light green) and $\text{D}_3^+ + \text{C}_2\text{N}^+$ (dark green) on the pump-probe delay axis. The projected signal intensity in (b) is normalized to 1 at 0 fs pump-probe delay for both H_3^+ and D_3^+ channels.

the dicationic state. That said, within the horizontal band, there is a strong dependence on the pump-probe delay. From the projection, shown in Fig. 2 (b), we see an enhancement in the total yield of this channel around time zero of the pump-probe delay due to the overlap of the two pulses. However, on either side of time zero, we see an immediate decrease in the yield before the signal steadily increases again. As discussed above, this behavior is the result of the disruptive nature of the probe pulse that prevents H_3^+ formation by ionizing the neutral roamer H_2 before it can abstract an H^+ . In other words, if the probe pulse arrives early enough, then it ‘disrupts’ the roaming H_2 , resulting in a decreased H_3^+ yield. For longer time delays, the probe pulse is less likely to disrupt H_2 roaming; thus, the yield of H_3^+ increases until reaching saturation.

We have additionally performed similar measurements using deuterated acetonitrile, which allows us to better resolve different masses when using ion time-of-flight spectroscopy. Overall, we observed no significant differences in the time-resolved measurements for either sample. This, in itself, is a rather interesting result since it reveals that the roaming process relies mostly on electronic properties rather than on nuclear dynamics. This is clearly illustrated in Fig. 2 (b), where we show the KER projections of the formation of both H_3^+ (light green line)

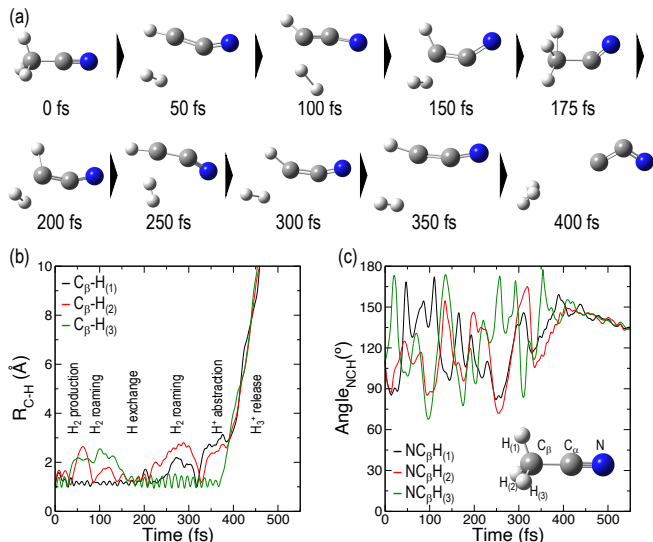


Figure 3. (a) Detailed analysis of a trajectory leading to the formation of H_3^+ . H_3^+ is formed as a result of roaming neutral H_2 followed by a proton abstraction. (b) Time-dependent change of the three C-H bond distances for the same trajectory used in (a), showing H_2 roaming and H abstraction leading to formation of H_3^+ . (c) Time-dependent change in the angle between NC_β and the three H atoms obtained from the same trajectory used in (a). In this trajectory, the three angles coincide around 400 fs implying ejection of H_3^+ . Acetonitrile molecule is shown in the inset identifying the labels for all the carbon and hydrogen atoms.

and D_3^+ (dark green line). The timescales of depletion and enhancement of the H_3^+ and D_3^+ projections are almost identical, thus showing that the process is independent of the mass of the roamer. Additionally, we have fitted the projections with a rising exponential of the form: $y = A(1 - e^{-(t-t_0)/\tau}) + y_0$ where A is the normalization constant, t is the pump-probe delay, t_0 is the time offset, τ is the time constant, and y_0 is the intensity offset. A and y_0 are arbitrary constants since the intensity is normalized to 1 at 0 fs pump-probe delay. However, t_0 and τ have physical significance since they reveal the timescales of the respective depletion and enhancement of the H_3^+ and D_3^+ formation. The values from the fitting function are given in Table S1 in the supplementary information (SI) while a comparison of the fits with the experimental data is given in Fig. S2 of the SI. The time offset, t_0 , has an average value of 125 fs, which is larger than the temporal resolution of the experiment (60 fs) and the time constant, τ has an average value of 105 fs. Overall, the fits reveal that H_2 roaming and H_3^+ formation occur on ultrafast timescales of a few hundred femtoseconds.

To better understand the mechanism of H_2 roaming and H_3^+ formation, we have performed molecular dynamics simulations, described in detail in the Methods section. We have found that the primary fragmentation channels producing cationic hydrogen species and

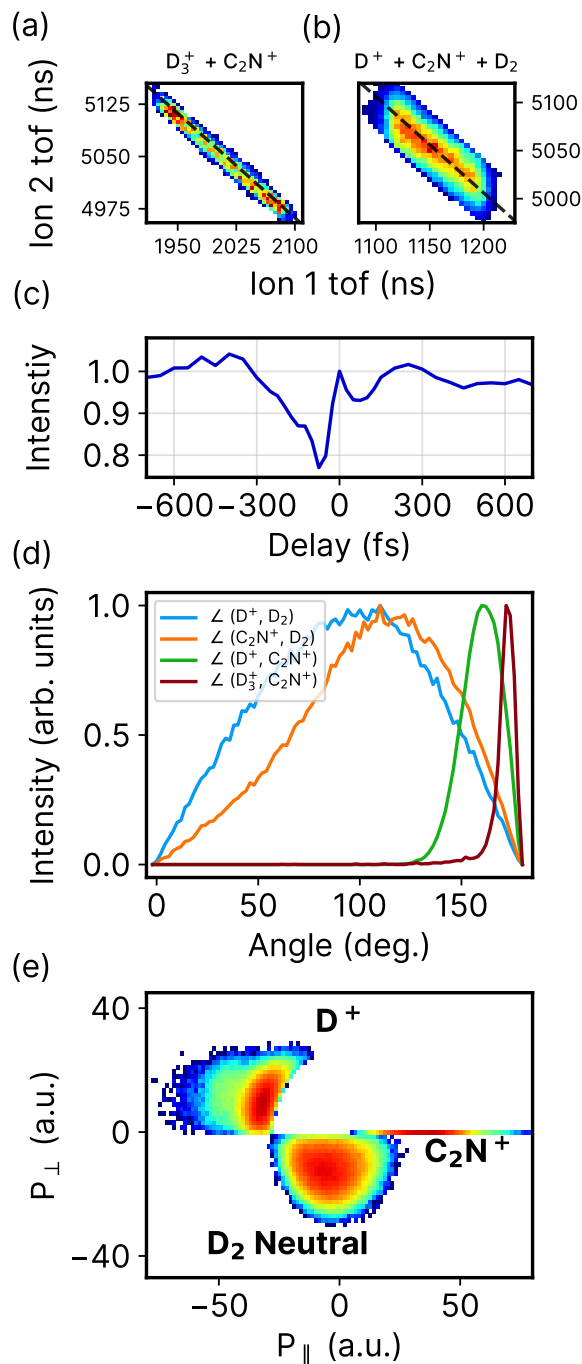


Figure 4. Photoion-photoion coincidence lines for (a) $D_3^+ + C_2N^+$ and (b) $D^+ + C_2N^+ + D_2$ from acetonitrile, integrated over all pump-probe delays. Black dashed lines of slope -1 are overlaid on the PIPICO channels (a) and (b) to demonstrate the agreement between the expected and experimentally-obtained slope of these channels. (c) Pump-probe delay-dependent kinetic energy projection of the roaming D_2 neutral. (d) Angular distribution between the momentum vectors of D^+ and D_2 (blue line), C_2N^+ and D_2 (orange line), D^+ and C_2N^+ (green line), and D_3^+ and C_2N^+ (crimson line) within the first 200 fs time-delay window. (e) Newton diagram for the channel $D^+ + D_2$ neutral + C_2N^+ integrated over the first 200 fs of pump-probe delay. The momentum vector of C_2N^+ lies along the x-axis while those of D^+ and D_2 neutral are plotted in the top and bottom halves, respectively.

their respective abundances are: $H^+/H_2C_2N^+$ - 79.6%, H_2^+/HC_2N^+ - 7.6%, and H_3^+/C_2N^+ - 0.8%. For the current work, we focus the analysis on those trajectories producing H_3^+ . Figure 3 shows the results from one of such trajectories leading to H_3^+ . Overall, several processes occur within the first few hundred femtoseconds which impact the H_3^+ formation. H_2 is produced in the first tens of fs and then roams around up to ~ 150 fs. Subsequently, H exchange occurs wherein the H atoms of the roaming H_2 molecule are bonded back to the carbon atom, immediately followed by a different pair of H atoms being ejected to form a new roaming H_2 molecule. After another ~ 200 fs, this H_2 molecule abstracts the last remaining H bonded to the C atom, thereby forming H_3^+ in coincidence with C_2N^+ . The plots in Fig. 3 (b) and (c) show time-evolution of the bond distances and angles of the three H atoms relative to the molecular skeleton of CCN for a typical trajectory. Results for the other trajectories are given in Figs. S3 and S4, and the corresponding variations of the nuclear kinetic energy with respect to time are given in Fig. S8. In all cases, H_3^+ is formed via neutral H_2 roaming, however, due to the small number of trajectories leading to H_3^+ , we cannot provide an exact value for the roaming time. That said, all simulated trajectories in the present work predict a formation timescale between 100 fs and 400 fs for H_3^+ , which overall agrees very well with the experimental measurements. The calculated nuclear kinetic energies in the final state are also in good agreement with the experimental KER (see Fig. S8).

In order to gain a detailed understanding of the roaming mechanism in acetonitrile, we track the dynamics of the neutral D_2 which appears in coincidence with D^+ and C_2N^+ using photoion-photoion coincidence (PIPICO) maps. In general, negative-sloping distributions observed in the PIPICO coincidence maps identify fragments created by multiple ionization. Specifically, the shape and slope of the distribution give information about the dissociation process [28]. For instance, the back-to-back emission of two ions, where momentum is conserved, results in a sharp line of slope -1. For deuterated acetonitrile, this is observed in Fig. 4 (a) for D_3^+ in coincidence with C_2N^+ . Prior to D_3^+ formation, the PIPICO channel that allows us to track the behavior of the neutral roamer is the incomplete channel of D^+ in coincidence with C_2N^+ , shown in Fig. 4 (b), which is missing the mass from D_2 . Incomplete coincidence channels can have unique shapes and slopes depending on the missing fragment [28]. When there is deferred charge separation of the different fragments with mass m such that a neutral m_3 is ejected first, followed by $m_1m_2^{2+}$ breaking apart into two ions, the resulting coincidence channel has a broad, lozenge shape of slope -1. This is precisely what we observe in Fig. 4 (b) for the channel $D^+ + C_2N^+ + D_2$. To show the agreement between the calculated slopes and experimental data, black dashed lines of slope -1 are overlaid

in the PIPICO channels in Figs. 4 (a) and (b), respectively. To further prove that the missing fragment in this channel is indeed neutral and not an ion that was simply lost in the detection process, we have plotted the kinetic energy of the missing D_2 in Fig. S5 of the SI. If it is an ion, one would observe a time-dependent decrease in its kinetic energy as a result of Coulomb explosion from the remaining charged moiety. On the other hand, a neutral dissociating from a charged fragment would result in very low, time-independent kinetic energy. The latter is observed in the reconstructed kinetic energy of D_2 , thus proving that the missing fragment is indeed neutral. Fig. 4 (c) shows the reconstructed kinetic energy projection of neutral D_2 as a function of pump-probe delay where the time-dependent behavior of this neutral fragment is similar to that of $H_3^+ + C_2N^+$, shown in Fig. 2 (b).

After isolating the coincidence channel involving the target neutral roamer D_2 , we then study its angular correlations with respect to the coincident ionic fragments. In Fig. 4 (d), we plot the angle between the momentum vectors of D_2 and D^+ (blue line), and D_2 and C_2N^+ (orange line). The momentum vector of D_2 , which is invisible to our detection scheme, is reconstructed by implementing momentum conservation among the three fragments. Overall, we see a very broad distribution implying a highly uncorrelated emission angle between the neutral D_2 and the two ionic fragments, which is a key signature of roaming. Unlike direct dissociation where the fragments follow a fixed minimum energy path, roaming fragments traverse relatively flat regions of the potential energy surface, which results in wide variations in their pathways. Such an uncorrelated behavior is exactly what makes roaming difficult to observe since the position of the roaming neutral is not well-defined as compared to a typical dissociation channel. In that regard, we have a potentially more direct method for visualizing roaming by directly mapping the momentum of the reconstructed neutral. For comparison, the ion-ion angular distribution for D^+ and C_2N^+ (green line) in this incomplete channel is much sharper and centered at $\sim 160^\circ$, indicating strong Coulomb interaction resulting in a stronger momentum correlation. Such an angular distribution between D^+ and C_2N^+ is also observed from the calculated roaming trajectories. For the trajectory shown in Fig. 3 (c), the angle between D^+ and C_2N^+ in the first 200 fs is approximately 150° with a dispersion around this value of the order of 30° . Finally, the angular distribution for D_3^+ and C_2N^+ (crimson line), which forms a complete two-body channel, is even narrower and centered at $\sim 175^\circ$ indicating back-to-back emission, as would be expected from a two-body fragmentation process.

Beyond examining simple angular correlations, we can also construct the full 3D momentum of the reaction, using Newton diagrams. In general, Newton diagrams are very useful tools for providing structural informa-

tion about the reaction dynamics of a system [29–31]. One of their unique features is the ability to distinguish different mechanisms of fragmentation. For instance, concerted, instantaneous fragmentation would appear as sharp, localized distributions in the Newton diagram [32], whereas sequential fragmentation would appear as a semicircle [31, 33] due to the rotation of the intermediate fragment whose lifetime is larger than its rotational period. A typical Newton diagram for a three-body fragmentation channel in acetonitrile, $D^+ + D_2^+ + C_2N^+$, is shown in Fig. S6 of the SI. In this case, the momentum distributions are sharp with strong angular correlations.

Figure 4 (e) shows the Newton diagram for the channel $D^+ + D_2$ neutral + C_2N^+ . Here, the pump-probe delay is constrained to values less than 200 fs. The momentum vector of C_2N^+ is fixed along the x-axis, while those of D^+ and the reconstructed D_2 are plotted on the top and bottom halves, respectively. Due to momentum conservation amongst the three fragments, the Newton diagram lies on a plane and shows the relative momentum distributions of two fragments with respect to C_2N^+ . Overall, there are several features that are markedly different from the analogous all-ion channel ($D^+ + D_2^+ + C_2N^+$), mentioned above. The distribution of the neutral D_2 in Fig. 4 (e) appears quite different from a typical fragmentation channel since there is no clear angular dependence in addition to a very broad, albeit lower momentum magnitude distribution. This shows that the neutral D_2 departs with a smaller fraction of the total momentum involved in this process, as would be expected from neutral fragmentation. It must be noted that, in sequential processes, rotation of the intermediate fragment can also result in broad angular distributions. Therefore, the Newton diagram in Fig. 4 (e) is integrated over the first 200 fs pump-probe delay window, which is much smaller than the rotational timescale for C_2ND^+ . Thus, the broad angular correlation that we observe here cannot be due to the rotation of the intermediate fragment C_2ND^+ , thereby removing any ambiguity between rotation and roaming. Such a lack of clear angular correlation in conjunction with a broad distribution of momentum magnitude of the neutral D_2 is a potentially unambiguous signature for roaming in molecules. Contrary to that, the two ions in this incomplete channel, D^+ and C_2N^+ , share a stronger momentum correlation mediated via Coulomb interaction as evidenced by a narrower angular spread along with a localized distribution in the magnitude of momentum.

To demonstrate how robust this method is for distinguishing neutral fragmentation channels, in Fig. S1 of the SI, we compare our results to a different type of neutral fragmentation, which was measured in 2-propanol ($CH_3CHOHCH_3$). In this case, the fragmentation channel, $CH_3^+ + H_2O$ neutral + $C_2H_5^+$, is initially two primary fragments, CH_3^+ and $C_2H_5O^+$, the latter of

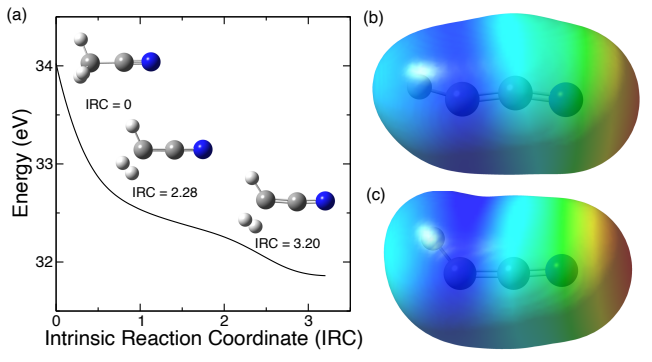


Figure 5. (a) Minimum Energy Path (MEP) followed in the potential energy surface of the doubly ionized acetonitrile; relative energy in eV referred to the neutral molecule as a function of the Intrinsic Reaction Coordinate (IRC). (b) and (c) Electrostatic potential (ESP) of HCCN^{2+} mapped on the electronic density with isovalue 0.0004 a.u.. Color code for the extreme values: red = 0.32 a.u. and dark blue = 0.48 a.u.. The geometry used in (b) corresponds to the channel $\text{H}_2/\text{HCCN}^{2+}$, i.e. after release of neutral H_2 , and in (c) to the weakly bonded $\text{H}_2\cdots\text{HCCN}^{2+}$, i.e. last point in the MEP.

which subsequently dissociates into C_2H_3^+ and neutral H_2O . In comparison to neutral roaming, we observe stark differences in the PIPICO channel, angular distributions, and Netwon diagram, which are discussed in detail in the SI.

Further insight into H_2 roaming has been obtained in a careful exploration of the potential energy surface (PES). In particular, we computed the minimum energy path (MEP) that a doubly charged acetonitrile molecule would follow after vertical ionization, i.e., the maximum gradient on the PES, starting from the optimized geometry of the neutral system (Fig. 5(a)). We clearly observe the release of neutral H_2 , followed by the production of a weakly bonded $\text{H}_2\cdots\text{HCCN}^{2+}$ complex. Furthermore, this shows that the neutral H_2 is polarized by the potential exerted by the cationic fragment. We evaluated such potential by computing the electrostatic potential (ESP) of HCCN^{2+} in two different configurations: using the geometry of the optimized structure from the moiety (Fig. 5(b)) and using the geometry of the last point given in the MEP exploration (Fig. 5(c)). The ESP is plotted in both cases by projecting the actual value on the electronic density isosurface, which provides a visualization of the potential that polarizes the neutral H_2 . Overall, Figs. 5 (b) and (c) reveal that the regions with the highest electrostatic potential (blue in color) are nearest to the C-H bond in HCCN^{2+} . It is most likely that the roaming H_2 remains weakly-bound in this region. Upon fragmentation of H^+ and CCN^+ , the H_2 is approximately at 90° with respect to the two ionic fragments, which qualitatively agrees with the angular correlations given in Fig. 4(d).

The fact that acetonitrile has only 3 hydrogen atoms

that can contribute to D_3^+ formation makes it an ideal candidate to unambiguously track such roaming reactions. However, in order to be exhaustive in terms of all the possible ways that D_3^+ can be formed in acetonitrile, we must also consider the possibility of a roaming neutral D which can abstract D_2 from the remaining moiety to form D_3^+ . For this, we have to consider the incomplete coincidence channel: $\text{D}_2^+ + \text{C}_2\text{N}^+ + \text{D}$. We note that the yield for this channel is nearly 4.5 times lower than $\text{D}^+ + \text{C}_2\text{N}^+ + \text{D}_2$, consequently making it a weak contributor to the D_3^+ channel. This is not surprising, since a free H or D atom is a radical, which makes it less likely to be formed than H_2 or D_2 . In fact, this channel is not observed in our theoretical simulations due to the limited number of trajectories used in the present work. To our knowledge, it has also not been observed in previous works. Following the same sequence as before, we first ensure that the missing D is indeed a neutral by looking at its kinetic energy as a function of time-delay. Furthermore, in Fig. S7, we show the angular correlation between all pairs of fragments in the channel $\text{D}_2^+ + \text{D neutral} + \text{C}_2\text{N}^+$. The broad and symmetric angular correlations between the neutral D and the other two ionic fragments are indications of roaming D. Unlike in Fig. 4, the correlation between D and C_2N^+ is quite symmetric. This could be a result of D being a lighter roaming fragment compared to D_2 .

CONCLUSION

In conclusion, we have developed a more direct means to image neutral roaming reactions in small molecular systems. Using ultrafast IR pump-IR probe spectroscopy combined with coincident Coulomb explosion imaging, we have time-resolved the formation of H_3^+ from neutral H_2 roaming in acetonitrile, which was measured to occur within a few hundred femtoseconds. This technique enables us to directly track the ‘invisible’ neutral roamer, the precursor to H_3^+ formation, from incomplete fragmentation channels. Additionally, with the aid of quantum chemistry calculations, we have fully simulated the possible roaming trajectories, allowing us to follow some of the unique intramolecular processes which occur in this type of dissociation. In general, our novel technique gives us a more straightforward means to observe neutral fragments which can allow us to gain a better understanding of the underlying molecular dynamics in roaming reactions.

METHODS

The experimental setup has been previously described elsewhere [34–36]. We used a 5 kHz Ti:Sapphire laser producing 35 fs pulses with a central wavelength of 800

nm. The laser beam was split into two independent arms which were time-delayed with respect to one another. Each arm had a variable intensity that was optimized to produce the highest contrast on the $\text{H}_3^+/\text{D}_3^+$ signal. For this experiment, the power was in the range of 10^{14} W/cm². The two beams were directed into the interaction region where they were overlapped and back-focused to a spot size of about 10 μm with a temporal resolution of about 60 fs. Both beams were linearly polarized in the direction of the time-of-flight axis of the spectrometer. A cold, molecular jet of acetonitrile, from a room-temperature bubbler, was produced by expansion through a 30 μm nozzle seeded with 1 bar of helium gas and propagated into the spectrometer perpendicular to the two laser pulses. Acetonitrile was ionized and resulting charged fragments were detected by a Cold Target Recoil Ion Momentum Spectrometer (COLTRIMS) [26, 27]. Using a weak, homogeneous electric field, the ions were directed towards a position-sensitive detector, which is capable of measuring the three-dimensional momentum distributions of the charged particles. For CEI, we primarily focus on measuring the fragmented ions, and for the current experimental conditions, we have an ion momentum resolution of 0.1 a.u. By applying the coincidence technique, we can isolate specific mass channels of acetonitrile and gain the most relevant information about the fragmentation dynamics.

Ab initio molecular dynamics simulations were performed, using the Atom Centered Density Matrix Propagation method (ADMP) [37–39] as implemented in the Gaussian16 program [40]. The electronic structure was computed, employing the density functional theory (DFT), in particular, the B3LYP functional [41, 42] in combination with the 6-31++G(d,p) basis set [43, 44]. To ensure the adiabaticity of the dynamics, we established a time step of $\Delta t = 0.1$ fs and a fictitious electron mass of $\mu = 0.1$ amu. Mimicking the experimental conditions, we considered a vertical double ionization of the acetonitrile molecule in a Franck–Condon manner, introducing a given amount of internal energy, $E_{exc} = 3$ eV, which was randomly redistributed over the nuclear degrees of freedom. This value was chosen to ensure that the energy available in the system agrees with the experimentally measured KER. 500 trajectories were propagated up to 1ps. We analyzed the statistical population of the different channels considering separated fragments with distances larger than 2.5 Å between atoms forming a moiety. Charges in the different atomic positions were computed from a Mulliken population analysis in the last step of each trajectory. We have successfully used this computational strategy in the past to infer the fragmentation dynamics in ionized molecules and clusters in the gas phase (see e.g. [34–36, 45–51]).

ACKNOWLEDGEMENTS

The experimental work was funded by the National Science Foundation under award No. 1700551. The theory was supported by the MICINN (Spanish Ministry of Science and Innovation) projects PID2019-105458RB-I00 and PID2019-110091GB-I00, funded by MCIN/AEI/10.13039/501100011033, the ‘Severo Ochoa’ Programme for Centres of Excellence in R&D (CEX2020-001039-S) and the ‘María de Maeztu’ Programme for Units of Excellence in R&D (CEX2018-000805-M). We acknowledge the generous allocation of computer time at the Centro de Computación Científica at the Universidad Autónoma de Madrid (CCC-UAM).

* These authors contributed equally.

- [1] J. M. Bowman and B. C. Shepler, *Annu. Rev. Phys. Chem.* **62**, 531 (2011).
- [2] J. M. Bowman and P. L. Houston, *Chem. Soc. Rev.* **46**, 7615 (2017).
- [3] A. G. Suits, *Annu. Rev. Phys. Chem.* **71** (2020).
- [4] D. Townsend, S. A. Lahankar, S. K. Lee, S. D. Chembreau, A. G. Suits, X. Zhang, J. Rheinecker, L. Harding, and J. M. Bowman, *Science* **306**, 1158 (2004).
- [5] P. Houston and S. Kable, *Proc. Natl. Acad. Sci. U.S.A.* **103**, 16079 (2006).
- [6] B. R. Heazlewood, M. J. Jordan, S. H. Kable, T. M. Selby, D. L. Osborn, B. C. Shepler, B. J. Braams, and J. M. Bowman, *Proc. Natl. Acad. Sci. U.S.A.* **105**, 12719 (2008).
- [7] S. Maeda, K. Ohno, and K. Morokuma, *J. Phys. Chem. Lett.* **1**, 1841 (2010).
- [8] M. P. Grubb, M. L. Warter, H. Xiao, S. Maeda, K. Morokuma, and S. W. North, *Science* **335**, 1075 (2012).
- [9] M. Nakamura, P.-Y. Tsai, T. Kasai, K.-C. Lin, F. Palazzetti, A. Lombardi, and V. Aquilanti, *Faraday Discuss.* **177**, 77 (2015).
- [10] A. Lombardi, F. Palazzetti, V. Aquilanti, H.-K. Li, P.-Y. Tsai, T. Kasai, and K.-C. Lin, *J. Phys. Chem. A* **120**, 5155 (2016).
- [11] A. K. Rauta and B. Maiti, *Chem. Phys. Lett.* **661**, 83 (2016).
- [12] N. Ekanayake, M. Nairat, B. Kaderiya, P. Feizollah, B. Jochim, T. Severt, B. Berry, K. R. Pandiri, K. D. Carnes, S. Pathak, *et al.*, *Sci. Rep.* **7**, 1 (2017).
- [13] N. Ekanayake, T. Severt, M. Nairat, N. P. Weingartz, B. M. Farris, B. Kaderiya, P. Feizollah, B. Jochim, F. Ziaee, K. Borne, *et al.*, *Nat. Commun.* **9**, 1 (2018).
- [14] E. Livshits, I. Luzon, K. Gope, R. Baer, and D. Strasser, *Communications Chemistry* **3**, 49 (2020).
- [15] Y. Furukawa, K. Hoshina, K. Yamanouchi, and H. Nakano, *Chem. Phys. Lett.* **414**, 117 (2005).
- [16] K. Hoshina, Y. Furukawa, T. Okino, and K. Yamanouchi, *J. Chem. Phys.* **129**, 104302 (2008).
- [17] K. Hoshina and M. Tsuge, *Chem. Phys. Lett.* **489**, 154 (2010).
- [18] P. M. Kraus, M. C. Schwarzer, N. Schirmel, G. Urbasch, G. Frenking, and K.-M. Weitzel, *J. Chem. Phys.* **134**,

- 114302 (2011).
- [19] T. Okino, A. Watanabe, H. Xu, and K. Yamanouchi, *Phys. Chem. Chem. Phys.* **14**, 4230 (2012).
- [20] N. Schirmel, N. Reusch, P. Horsch, and K.-M. Weitzel, *Faraday Discuss.* **163**, 461 (2013).
- [21] N. Kotsina, S. Kaziannis, and C. Kosmidis, *Int. J. Mass Spectrom.* **380**, 34 (2015).
- [22] T. Geballe and T. Oka, *Nature* **384**, 334 (1996).
- [23] B. McCall, T. Geballe, K. Hinkle, and T. Oka, *Science* **279**, 1910 (1998).
- [24] E. Herbst and W. Klemperer, *Astrophys. J.* **185**, 505 (1973).
- [25] T. Endo, S. P. Neville, V. Wanie, S. Beaulieu, C. Qu, J. Deschamps, P. Lassonde, B. E. Schmidt, H. Fujise, M. Fushitani, *et al.*, *Science* **370**, 1072 (2020).
- [26] J. Ullrich, R. Moshhammer, R. Dörner, O. Jagutzki, V. Mergel, H. Schmidt-Böcking, and L. Spielberger, *J. Phys. B: At., Mol. Opt. Phys.* **30**, 2917 (1997).
- [27] J. Ullrich, R. Moshhammer, A. Dorn, R. Dörner, L. P. H. Schmidt, and H. Schmidt-Böcking, *Rep. Prog. Phys.* **66**, 1463 (2003).
- [28] J. Eland, *Laser Chem.* **11**, 259 (1991).
- [29] R. Boll, J. M. Schäfer, B. Richard, K. Fehre, G. Kastirke, Z. Jurek, M. S. Schöffler, M. M. Abdullah, N. Anders, T. M. Baumann, *et al.*, *Nat. Phys.* **18**, 423 (2022).
- [30] S. Bhattacharyya, K. Borne, F. Ziaee, S. Pathak, E. Wang, A. S. Venkatachalam, X. Li, N. Marshall, K. D. Carnes, C. W. Fehrenbach, *et al.*, *J. Phys. Chem. Lett.* **13**, 5845 (2022).
- [31] S. Pathak, R. Obaid, S. Bhattacharyya, J. Bürger, X. Li, J. Tross, T. Severt, B. Davis, R. C. Bilodeau, C. A. Trallero-Herrero, *et al.*, *J. Phys. Chem. Lett.* **11**, 10205 (2020).
- [32] X. Xie, C. Wu, Y. Yuan, X.-Z. Li, C. Wu, P. Wang, Y. Deng, Y. Liu, and Q. Gong, *AIP Adv.* **5**, 097213 (2015).
- [33] N. Neumann, D. Hant, L. P. H. Schmidt, J. Titze, T. Jahnke, A. Czasch, M. Schöffler, K. Kreidi, O. Jagutzki, H. Schmidt-Böcking, *et al.*, *Phys. Rev. Lett.* **104**, 103201 (2010).
- [34] N. G. Kling, S. Díaz-Tendero, R. Obaid, M. Disla, H. Xiong, M. Sundberg, S. Khosravi, M. Davino, P. Drach, A. Carroll, *et al.*, *Nat. Commun.* **10**, 1 (2019).
- [35] M. McDonnell, A. C. LaForge, J. Reino-Gonzalez, M. Disla, N. G. Kling, D. Mishra, R. Obaid, M. Sundberg, V. Svoboda, S. Díaz-Tendero, *et al.*, *J. Phys. Chem. Lett.* **11**, 6724 (2020).
- [36] D. Mishra, J. Reino-González, R. Obaid, A. C. LaForge, S. Díaz-Tendero, F. Martín, and N. Berrah, *Phys. Chem. Chem. Phys.* **24**, 433 (2022).
- [37] H. B. Schlegel, J. M. Millam, S. S. Iyengar, G. A. Voth, A. D. Daniels, G. E. Scuseria, and M. J. Frisch, *J. Chem. Phys.* **114**, 9758 (2001).
- [38] S. S. Iyengar, H. B. Schlegel, J. M. Millam, G. A. Voth, G. E. Scuseria, and M. J. Frisch, *J. Chem. Phys.* **115**, 10291 (2001).
- [39] H. B. Schlegel, S. S. Iyengar, X. Li, J. M. Millam, G. A. Voth, G. E. Scuseria, and M. J. Frisch, *J. Chem. Phys.* **117**, 8694 (2002).
- [40] M. J. Frisch, G. W. Trucks, H. B. Schlegel, G. E. Scuseria, M. A. Robb, J. R. Cheeseman, G. Scalmani, V. Barone, G. A. Petersson, H. Nakatsuji, X. Li, M. Caricato, A. V. Marenich, J. Bloino, B. G. Janesko, R. Gomperts, B. Mennucci, H. P. Hratchian, J. V. Ortiz, A. F. Izmaylov, J. L. Sonnenberg, D. Williams-Young, F. Ding, F. Lipparini, F. Egidi, J. Goings, B. Peng, A. Petrone, T. Henderson, D. Ranasinghe, V. G. Zakrzewski, J. Gao, N. Rega, G. Zheng, W. Liang, M. Hada, M. Ehara, K. Toyota, R. Fukuda, J. Hasegawa, M. Ishida, T. Nakajima, Y. Honda, O. Kitao, H. Nakai, T. Vreven, K. Throssell, J. A. Montgomery, Jr., J. E. Peralta, F. Ogliaro, M. J. Bearpark, J. J. Heyd, E. N. Brothers, K. N. Kudin, V. N. Staroverov, T. A. Keith, R. Kobayashi, J. Normand, K. Raghavachari, A. P. Rendell, J. C. Burant, S. S. Iyengar, J. Tomasi, M. Cossi, J. M. Millam, M. Klene, C. Adamo, R. Cammi, J. W. Ochterski, R. L. Martin, K. Morokuma, O. Farkas, J. B. Foresman, and D. J. Fox, “Gaussian16 Revision C.01,” (2016), gaussian Inc. Wallingford CT.
- [41] A. D. Becke, *J. Chem. Phys.* **98**, 5648 (1993), <https://doi.org/10.1063/1.464913>.
- [42] C. Lee, W. Yang, and R. G. Parr, *Phys. Rev. B* **37**, 785 (1988).
- [43] T. Clark, J. Chandrasekhar, G. W. Spitznagel, and P. V. R. Schleyer, *J. Comput. Chem.* **4**, 294 (1983).
- [44] R. Krishnan, J. S. Binkley, R. Seeger, and J. A. Pople, *J. Chem. Phys.* **72**, 650 (1980).
- [45] S. Maclot, D. G. Piekarski, A. Domaracka, A. Meéry, V. Vizcaino, L. Adoui, F. Martín, M. Alcamí, B. A. Huber, P. Rousseau, *et al.*, *J. Phys. Chem. Lett.* **4**, 3903 (2013).
- [46] E. Kukk, D. Ha, Y. Wang, D. G. Piekarski, S. Díaz-Tendero, K. Kooser, E. Itälä, H. Levola, M. Alcamí, E. Rachlew, and F. Martín, *Phys. Rev. A* **91**, 043417 (2015).
- [47] D. G. Piekarski, R. Delaunay, S. Maclot, L. Adoui, F. Martín, M. Alcamí, B. A. Huber, P. Rousseau, A. Domaracka, and S. Díaz-Tendero, *Phys. Chem. Chem. Phys.* **17**, 16767 (2015).
- [48] S. Maclot, R. Delaunay, D. G. Piekarski, A. Domaracka, B. Huber, L. Adoui, F. Martín, M. Alcamí, L. Avaldi, P. Bolognesi, *et al.*, *Phys. Rev. Lett.* **117**, 073201 (2016).
- [49] P. Rousseau, D. G. Piekarski, M. Capron, A. Domaracka, L. Adoui, F. Martin, M. Alcamí, S. Diaz-Tendero, and B. A. Huber, *Nat. Commun.* **11**, 3818 (2020).
- [50] D. Barreiro-Lage, P. Bolognesi, J. Chiarinelli, R. Richter, H. Zettergren, M. H. Stockett, L. Carlini, S. Diaz-Tendero, and L. Avaldi, *J. Phys. Chem. Lett.* **12**, 7379 (2021).
- [51] S. Ganguly, D. Barreiro-Lage, N. Walsh, B. Oostenrijk, S. t. L. Sorensen, S. Diaz-Tendero, and M. Gisselbrecht, *Commun. Chem.* **5**, 16 (2022).

Supplemental Information for – Direct visualization of an elusive molecular reaction: Time-resolved H₂ roaming in acetonitrile

Debadarshini Mishra*^{†,1} Aaron C. LaForge*^{†,1} Lauren M. Gorman,¹
Sergio Díaz-Tendero,^{2,3,4} Fernando Martín,^{2,3,5} and Nora Berrah¹

¹*Department of Physics, University of Connecticut, Storrs, Connecticut, 06269, USA*

²*Departamento de Química, Módulo 13, Universidad Autónoma de Madrid, 28049 Madrid, Spain, EU*

³*Condensed Matter Physics Center (IFIMAC), Universidad Autónoma de Madrid, 28049 Madrid, Spain, EU*

⁴*Institute for Advanced Research in Chemical Sciences (IAdChem),*

Universidad Autónoma de Madrid, 28049 Madrid, Spain

⁵*Instituto Madrileño de Estudios Avanzados en Nanociencia (IMDEA-Nano),
Campus de Cantoblanco, 28049 Madrid, Spain, EU*

NEUTRAL FRAGMENTATION CHANNEL IN 2-PROPANOL

In order to fully demonstrate the differences between a roaming and non-roaming neutral fragmentation channel, we have plotted in Fig. S1 the relevant dynamics from CH₃⁺ + H₂O neutral + C₂H₃⁺ in 2-propanol (CH₃CHOHCH₃). The PIPICO channel, shown in Fig. S1 (a), is for CH₃⁺ measured in coincidence with C₂H₃⁺, with a missing mass of H₂O. This channel involves two primary fragments, CH₃⁺ and C₂H₅O⁺, the latter of which subsequently dissociates into C₂H₃⁺ and neutral H₂O, with a slope that can be calculated as $-m_{C_2H_3^+}/(m_{C_2H_3^+} + m_{CH_3^+}) = -0.643$ [?]. A black dashed line of slope -0.643 is overlaid on this PIPICO channel to demonstrate the agreement between the expected and experimentally-obtained slope. Fig. S1 (b) shows the angular correlations between the momentum vectors of neutral H₂O and C₂H₃⁺ (blue line) and neutral H₂O and CH₃⁺ (orange line). Both these distributions are asymmetrically shifted either towards or away from 0° implying stronger momentum correlation, further corroborating that the neutral fragmentation of H₂O proceeds through a secondary decay from C₂H₅O⁺. This behavior is in sharp contrast to that of corresponding angular distributions observed for the roaming neutral D₂ (shown to the right for comparison). Additionally, Fig. S1 (c) shows the Newton diagram for this channel over the first 200 fs pump-probe delay window. Here, the momentum vector of C₂H₃⁺ is fixed along the x-axis, while those of CH₃⁺ and the reconstructed H₂O are plotted on the top and bottom halves, respectively. Although the ionic fragments, C₂H₃⁺ and CH₃⁺, share similar characteristics to their counterparts in deuterated acetonitrile (shown to the right), the neutral fragments are significantly different. Specifically, the reconstructed momentum of neutral H₂O is strongly directed towards C₂H₃⁺, which fully supports that H₂O is produced through a secondary decay from C₂H₅O⁺. On the other hand, the reconstructed momentum of neutral D₂ displays no such preferential angularity and has a broad distribution centered at low momentum.

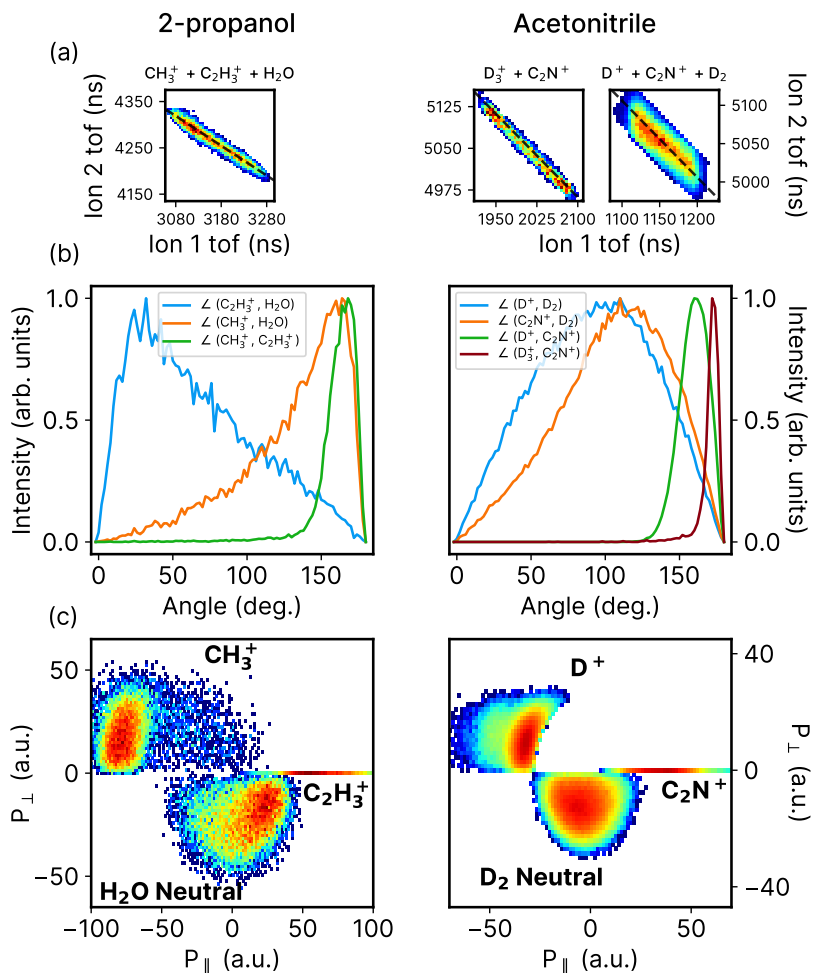


Figure S1. (a) Incomplete PIPICO channel for $\text{CH}_3^+ + \text{H}_2\text{O neutral} + \text{C}_2\text{H}_3^+$ from 2-propanol integrated over the first 200 fs. A black dashed line of slope -0.643 is overlaid on the PIPICO channel to show the agreement between the calculated slope and experimental coincidence channel. (b) Angular distributions between the momentum vectors of C_2H_3^+ and H_2O (blue line), CH_3^+ and H_2O (orange line), CH_3^+ and C_2H_3^+ (green line) within the first 200 fs time-delay window. (c) Newton plot for the channel $\text{CH}_3^+ + \text{C}_2\text{H}_3^+ + \text{H}_2\text{O neutral}$ integrated over the first 200 fs of pump-probe delay. The momentum vector of C_2H_3^+ lies along the x-axis while those of CH_3^+ and $\text{H}_2\text{O neutral}$ are plotted in the top and bottom halves, respectively. Fig. 4 from the main text is shown in the right column for comparison to acetonitrile.

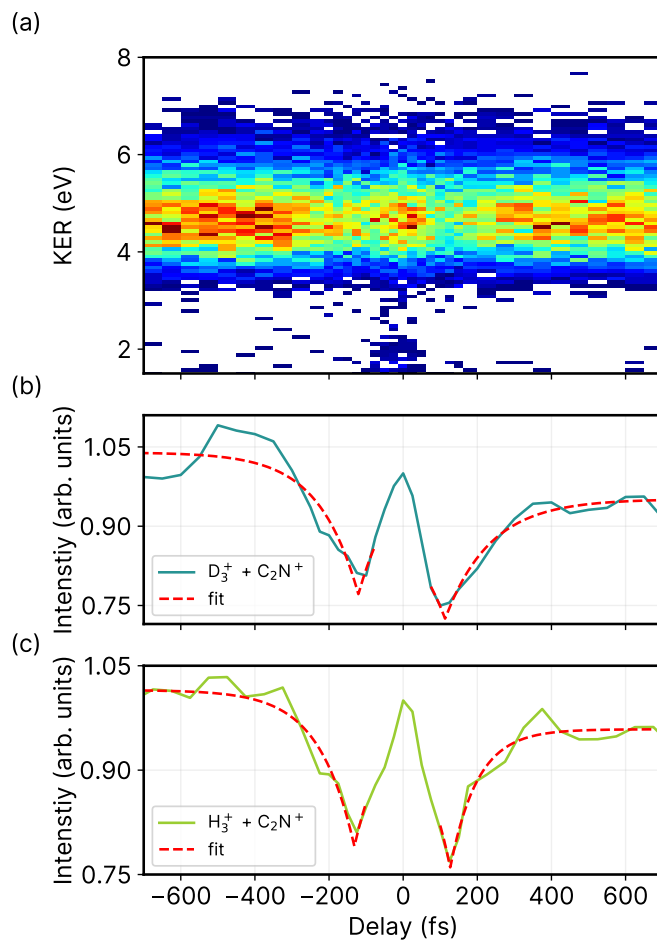


Figure S2. (a) Kinetic energy release of $D_3^+ + C_2N^+$. Projection of KER for (b) $D_3^+ + C_2N^+$ and (c) $H_3^+ + C_2N^+$ on the pump-probe delay axis. Red dashed lines obtained from the fit function (mentioned in the main text) are overlaid for comparison. The values from the fitting function are given in Table S1.

Table S1. Fit values

Signal	t_0	τ
H_3^+ Neg Delay	-131 ± 6 fs	111 ± 23 fs
H_3^+ Pos Delay	127 ± 6 fs	75 ± 20 fs
D_3^+ Neg Delay	-121 ± 10 fs	105 ± 30 fs
D_3^+ Pos Delay	113 ± 5 fs	122 ± 25 fs

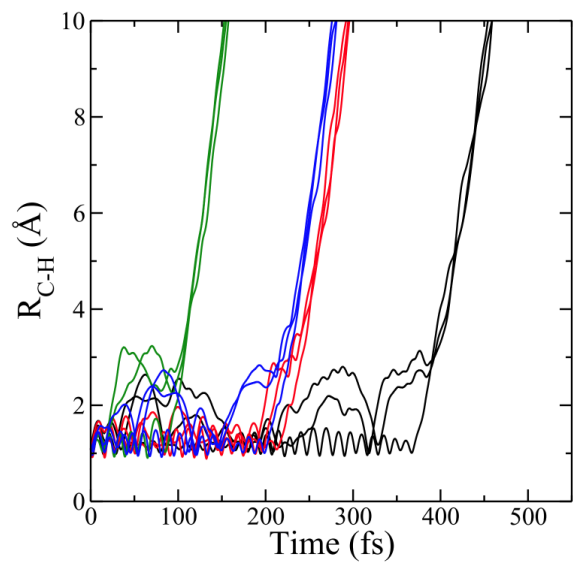


Figure S3. Distance between the terminal carbon atom and each hydrogen atom (in \AA) as a function of the time in the trajectories of the molecular dynamics simulations leading to H_3^+ . The three C-H distances in each trajectory are given in different colors.

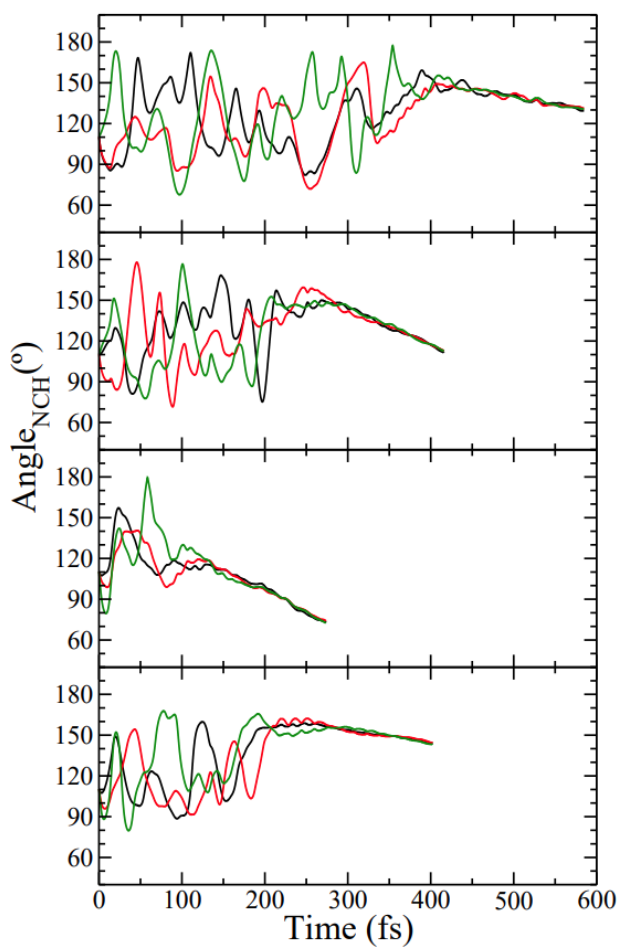


Figure S4. Angle formed by the nitrogen, terminal carbon and hydrogen atoms (in degrees) as a function of the time in the trajectories of the molecular dynamics simulations leading to H_3^+ . The angle for each hydrogen atom is given in a different color in the trajectory.

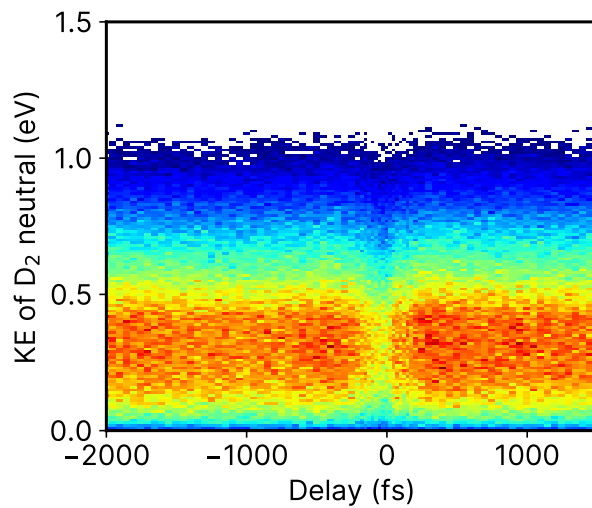


Figure S5. Kinetic energy of the neutral D_2 from the channel $\text{D}^+ + \text{C}_2\text{N}^+ + \text{D}_2$.

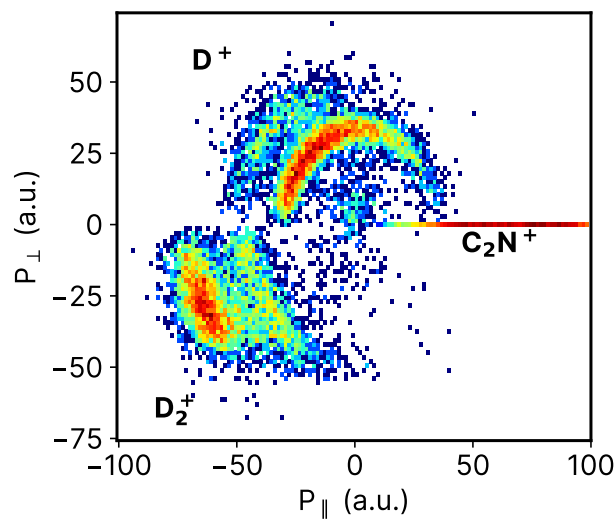


Figure S6. Newton plots for the channel $D^+ + D_2^+ + C_2N^+$ integrated over 200 fs time-delay window. The momentum vector of C_2N^+ is fixed along the x-axis and the momentum vectors of D^+ and D_2^+ are plotted in the upper and lower halves of the plot, respectively.

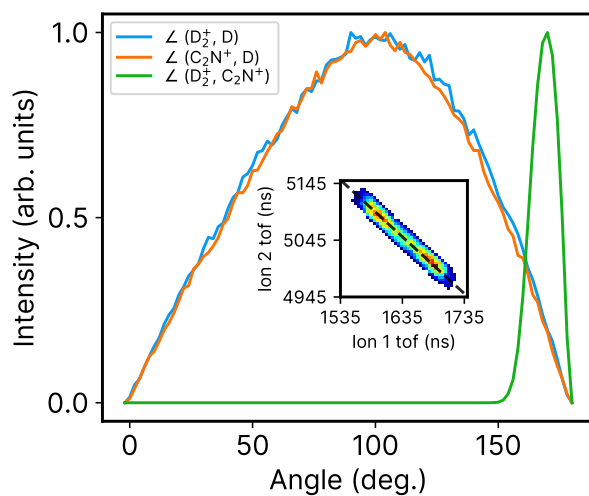


Figure S7. Angular distributions between pairs of fragments in the incomplete $D_2^+ + C_2N^+ + D$ channel

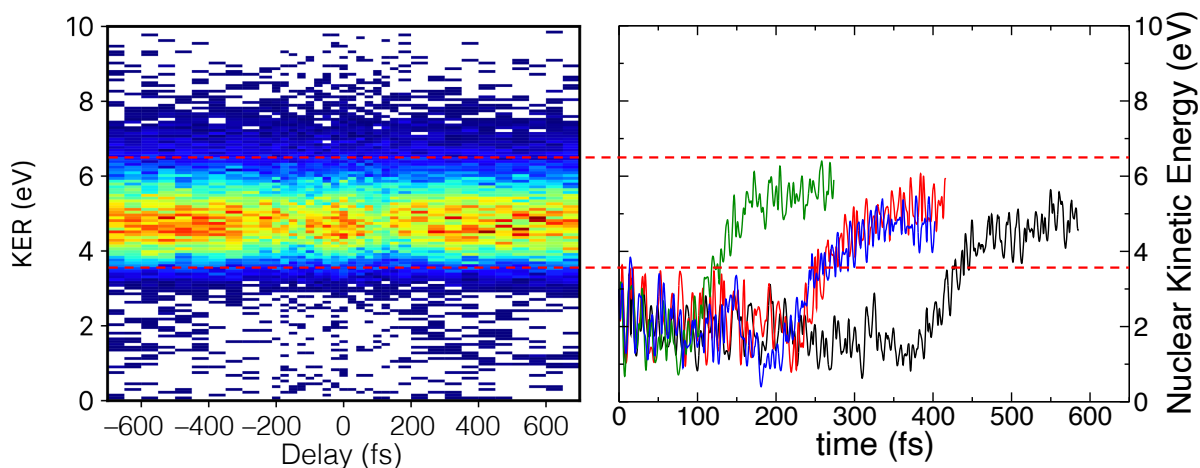


Figure S8. Nuclear kinetic energy as a function of time for the four trajectories leading to $\text{H}_3^+ + \text{C}_2\text{N}^+$.

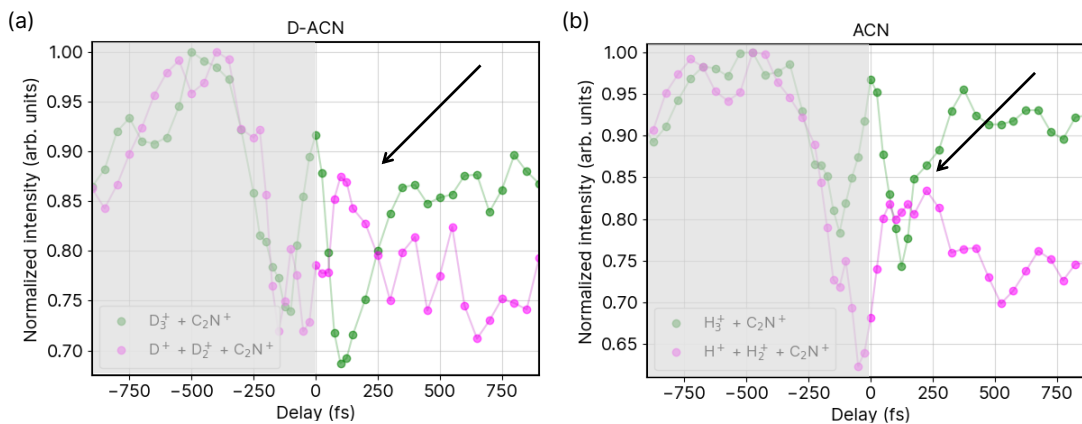


Figure S9. Correlation between two-body ($\text{D}_3^+ + \text{C}_2\text{N}^+$ and three-body ($\text{D}^+ + \text{D}_2^+ + \text{C}_2\text{N}^+$) time-dependent KER dynamics in (a) deuterated acetonitrile and (b) acetonitrile. It is noted that the pump and probe pulses have slightly different beam diameters and pulse energies, and thus have different pulse intensities. For this measurement, positive delays have a stronger probe pulse than the pump pulse, and vice versa for negative delays. For positive delays, there is a correlated relationship between the double and triple ionization yields, which verifies that the depleted doubly ionized channel results in an enhancement of the triply ionized channel. For negative delays, both the double and triply ionized channels have the same time dependence. We believe this is due to the weaker probe pulse, which does not sufficiently ionize the neutral fragments.

* contributed equally

† To whom correspondence should be addressed. Email: debadarshini.mishra@uconn.edu or aaron.laforge@uconn.edu